Thermodynamics and kinetics of homogeneous crystal nucleation studied by computer simulation

H. E. A. Huitema,[1] J. P. van der Eerden,[1] J. J. M. Janssen,[2] and H. Human[2]
[1]*Department of Interfaces, Debye Institute, Utrecht University, Padualaan 8, 3584 CH Utrecht, The Netherlands*
[2]*Unilever Research Vlaardingen, Olivier van Noortlaan 120, 3133 AT Vlaardingen, The Netherlands*
(Received 3 March 2000; revised manuscript received 1 June 2000)

Crystal nucleation is numerically simulated in the Lennard-Jones model. By isobaric cooling and isothermal compression of a liquid, we succeeded in fully crystallizing a large number of systems containing up to 10 000 atoms. We assessed thermodynamic data (density, enthalpy, and chemical potential) of the crystalline as well as the (metastable) liquid phase for considerably larger ranges of pressure and temperature than published so far. Using these data, we were able to confront our simulation results with classical nucleation theories without the need to recognize a critical cluster during the simulations. One of the findings is that in our experiments the steady-state nucleation regime was almost never reached. Careful analysis resulted in an estimate of the time-dependent effects in the nucleation rate, during which the nucleation rate grows from zero to its steady-state value. This way we were able to determine the values of the steady-state nucleation rate, which are consistent with independent estimates for both the preexponential factor and the nucleation barrier. In most previous experimental and simulation studies by other research groups, preexponential factors have been found that are orders of magnitude too large or too small. Our investigations show that an important factor in this discrepancy could be due to an underestimation of time-dependent nucleation effects.

I. INTRODUCTION

Classical nucleation theory is a phenomenological theory describing the onset of formation of a new stable phase from a metastable phase.[1,2] For crystal nucleation of undercooled liquids, the description is based on spherical clusters of the solid phase that form spontaneously and, when reaching a critical size, grow to form the new, stable phase. The nucleation process is described as an activated process with a free energy barrier separating the two phases. The height of the barrier is determined by two factors: the chemical potential difference between the molecules of the two phases and the interfacial free energy between the cluster of the new phase and the liquid. A cluster of critical size is at the top of the free energy barrier.

The rate at which a cluster changes size is determined by a kinetic coefficient, called the preexponential factor in classical nucleation theory. This coefficient together with the free energy barrier determines the time scale for the nucleation process. At small undercooling the nucleation rate is negligible, because the free energy barrier for the formation of a critical cluster is too high, while at large undercooling the nucleation rate is lowered because of the low value of the kinetic coefficient (i.e., the decreasing mobility of the molecules). Between these two limits nucleation of the crystalline phase from the undercooled liquid is observed.

It is difficult to measure the nucleation rate experimentally.[1] It is hard to count the number of nuclei that form and most importantly to distinguish homogeneous from heterogeneous nucleation. In computer simulations heterogeneous nucleation can be prevented by performing simulations without container walls (e.g., applying periodic boundary conditions) and without any impurities. This is a big advantage for quantitative measurements of the homogeneous nucleation rate. Comparison with nucleation theory can then be made by determination of the relevant thermodynamic parameters, something that can be done very accurately by computer simulation.[3]

The most important disadvantages of computer simulations are the small number of molecules (about 10^4) and simulation time (about 10^{-8} s). This limits the measurable nucleation rate to large values compared to experimental situations, where a number of molecules in the order of moles and a physical time in the order of hours are used. When comparing the results of computer simulations with nucleation theory, one therefore has to bear in mind that steady-state theories might fail to describe the results quantitatively.

Nucleation induced by undercooling a liquid has been the subject of many computer simulation studies over the last decades.[4,5] An observation of the nucleation of the crystalline phase in three dimensions during a computer simulation was by Rahman *et al.* in an amorphous Lennard-Jones system.[6] Subsequently, a large number of simulation studies concerning the homogeneous nucleation process have been reported.[7–14] All of these studies are concerned with spontaneous nucleation by undercooling a liquid, because it is a common experimental situation. To our knowledge only Nosé and Yonezawa[12,13] used constant-pressure conditions, while all others used constant-volume or -energy conditions that are more difficult to compare with experimental situations.

The most important problem hampering comparison between the simulation results and nucleation theory is the small number of samples crystallized, resulting in a large error in the measured nucleation rate of a specific sample. The fast increase in computational power enabled us to gain the required statistics about the nucleation rate over a wide range in temperature and pressure by performing a large number of homogeneous nucleation simulations where a liquid is cooled or compressed at different conditions. The time at which nucleation took place during these simulations is

estimated by heating of the cooled systems and decompression of the compressed systems at a number of points. This way we are able to quantitatively compare simulation data with predictions from nucleation theory over a wide range in temperature and pressure, without the need to recognize (or define) a critical cluster during the simulations.

The outline of this paper is as follows. We start by computing the thermodynamic and kinetic parameters needed for the expressions of nucleation theory from simulations of bulk liquid and crystal systems. This is followed by a large number of simulations where a liquid is isobarically cooled and subsequently heated or isothermally compressed and subsequently decompressed at different start and end points in the phase diagram. The cooling and compression rate are also varied, thereby probing the time-dependent effects in the nucleation rate.

The simulation results are confronted with (semi)empirical fit equations, steady-state classical nucleation rate equations, and time-dependent nucleation rate equations. The steady-state equations already give a reasonable qualitative description of results obtained, even though non-steady-state effects are important. The time-dependent equations, on the other hand, show an excellent agreement with our data while using only a small number of adjustable parameters.

Our final expression for the nucleation rate is compared with the experimental results of Brugmans and Vos[15] showing the importance of time-dependent effects during nucleation. Another comparison is made with the value of the steady-state nucleation rate for the Lennard-Jones system determined by ten Wolde *et al.* and others[16–20] showing good agreement. The differences result in an error estimate for both our and their method.

II. METHOD

The Lennard-Jones interaction potential was used, multiplied by a cutoff function to force the potential to zero at a distance beyond 2.5σ from the center of mass of the atoms while the value and position of the minimum of the Lennard-Jones interaction potential are unaffected:

$$V_{\mathrm{LJ}}(r)=4\varepsilon\left[\left(\frac{\sigma}{r}\right)^{12}-\left(\frac{\sigma}{r}\right)^{6}\right]f^{\mathrm{CO}}(r), \tag{1}$$

with

$$f^{\mathrm{CO}}(r)=1.199\exp\left(\frac{0.25\sigma}{r-2.5\sigma}\right)$$

for $r<2.5\sigma$ and $f^{\mathrm{CO}}(r)=0$ for $r\geqslant 2.5\sigma$.

The values of the two parameters ε and σ are tuned to argon: $\varepsilon/k=114.1\,\mathrm{K}$ and $\sigma=0.3405\,\mathrm{nm}$. Periodic boundary conditions are applied to all three dimensions. The simulations are carried out in the isothermal-isobaric ensemble (e.g., constant pressure, temperature, and number of atoms).

The velocity-Verlet[21] integration scheme with a time step of 0.015 ps is used for the molecular dynamics (MD) simulations. The thermostat is a Monte Carlo velocity scaling move introduced by Heyes[22] that is applied once in every four sweeps on average with an acceptance ratio of 0.2–0.4. The manostat is the Monte Carlo volume scaling process[3] using an algorithm similar to that of the thermostat and applied with the same frequency and acceptance ratio.

A. Thermodynamic and self-diffusion measurements

For the thermodynamic measurements, 92 equilibrium MD simulations of a bulk fcc solid, 87 of a bulk liquid, and 10 of a bulk amorphous solid (i.e., a glass) were performed at different (T,P) conditions. The system used for the solid consisted of a rectangular box containing $6\times6\times6$ unit cells (i.e., 864 atoms). For the liquid and glass a system containing 2000 atoms was used. The simulations for the liquid and solid all started with an equilibration period of 60 ps followed by 500 measurements in 150 ps simulation time. The starting configuration for the simulations of the glass phase was obtained from a well-equilibrated stable liquid that was quenched instantaneously. The simulations for the glass started with an equilibration period of 75 ps followed by 166 measurements in 75 ps time. The results for the simulations of the liquid and glass were used together in one fit that was accurate in regions close to the melting curve as well as for deeply quenched liquids, transforming into a glass.

Measurements of the potential energy per atom (u) and number density (ρ) were performed, while the temperature (T) and pressure (P) were set. The enthalpy per atom (h) is obtained from the potential energy and the density by

$$h=u+\frac{P}{\rho}+\frac{3}{2}T. \tag{2}$$

Based on these measurements fits of the chemical potential, the pressure and enthalpy as function of the temperature and density were created for the solid as well as the liquid and glass phases, using a total of 15 fit parameters per phase. Details on the fit expressions and the values of the fit parameters can be found in Appendix A.

The liquid self-diffusion coefficient (D) was also measured during the bulk liquid simulations by use of the Einstein relationship[23]

$$D=\lim_{t\to\infty}\frac{1}{6t}\langle\Delta r^2(t)\rangle, \tag{3}$$

where $\langle\Delta r^2(t)\rangle$ is the mean-square displacement per atom as function of time. We used the average slope of $\langle\Delta r^2(t)\rangle/6$ over the last 150 ps simulation time as the value of D. These measurements were used to fit the self-diffusion coefficient as a function of the temperature and density with an equation containing 12 fit parameters that is closely linked to the Arrhenius relationship, describing the self-diffusion of the Lennard-Jones liquid at constant pressure very well.[24,25] Details of the fit expressions and values of the fit parameters can be found in Appendix B.

All fit procedures were performed with use of the Minpack nonlinear optimization package.[26]

B. Homogeneous crystal nucleation simulations

For cooling, heating, compression, and decompression simulations, a system identical to the system used for the thermodynamic measurements in the liquid phase was used. We applied a linear change in time of the temperature or

pressure during the cooling or compression stages and an identical but opposite change during the heating or decompression stages. Several checks were made to ensure that the temperature and pressure during the simulations were identical to the applied values (except for the statistical noise) during all simulation runs.

For the cooling and heating runs the start configuration was first equilibrated in the stable liquid region of the phase diagram and subsequently cooled below the melting point at a constant cooling rate to a minimum temperature. At two to four points during the cooling stage, a configuration was taken as the start of a simulation where the system was heated at the same rate to a temperature at 10% undercooling ($T=0.9T_m$). The pressure, the initial and minimum temperature, and cooling rate were varied between the cooling runs. A total of 82 cooling runs were performed, divided over five different pressures: $P=0.001$, 1, 3, 5, and 8 katm. The total number of heating runs started from these cooling runs was 230.

For the compression-decompression runs the starting configuration was equilibrated the same way. Next, the system was compressed at a constant rate to a maximum pressure. At two to four points during the compression stage, a configuration was taken as the start of a decompression run at the same rate to a pressure at 10% undercooling. A total of 72 compression runs were performed, divided over five different temperatures: $T=70$, 85, 100, 120, and 140 K. The total number of decompression runs started from these compression runs was 226.

At the end of the runs (at 10% undercooling) the state of the system was examined by comparison between the measured density and energy of the system with the values of the thermodynamic fit equations. This resulted in one outcome, denoted by P_n^i, per heating-decompression run i, either being 0 if the system stayed in the liquid phase or 1 if the system transformed into the crystalline phase. The large number of simulation runs $(230+226)$ enabled us to gain the required statistics to confront our results with nucleation theory without the need to recognize the critical cluster during the simulations.

C. Nucleation probability distribution function

The nucleation probability over the complete simulation run is related to the nucleation rate at every point during the run by the following first-order differential equation:

$$\frac{\partial p_0(t)}{\partial t} = -VI(t)p_0(t), \tag{4}$$

where $VI(t)$ is the nucleation rate per unit time for the system at the (P,T) conditions of time t and p_0 is the probability that the system is still in the liquid phase. Together with $p_0(0)=1$ (i.e., we always start in the liquid phase) this results in the following expression for the nucleation probability distribution function (PDF) p_n:

$$p_n(t)=1-p_0(t)=1-\exp\left(-\int_0^t VI(t')dt'\right). \tag{5}$$

When comparing the value of the nucleation PDF with the results of the simulation runs, the integration is only performed up to time $t_{1/2}$, where the system is at maximum undercooling or compression. It is our opinion that during the heating or decompression stages the nucleation probability is much lower, because the critical cluster size is increasing in time, but we have to bear in mind that the preexponential factor we find contains a (small) uncertainty of at most a factor of 2. The integral in Eq. (5) was numerically integrated using a time step $dt=2.5$ ps.

The results of the simulation runs were fit in a least-squares sense to the nucleation PDF of Eq. (5), minimizing the quantity S_{P_n}:

$$S_{P_n}=\frac{1}{N}\sum_{i=1}^{N}[p_n(t_{1/2}^i)-P_n^i]^2, \tag{6}$$

where $N=556$ (i.e., the total number of cooling-heating plus compression-decompression simulation runs).

D. Classical nucleation theory

Classical nucleation theory will be used as the link between the measurements of the nucleation probability and thermodynamic measurements. The classical steady-state nucleation rate (I^S) is expressed in the Becker-Döring formalism as[1,27]

$$I^S=\omega^* Z N_{n^*}^{\mathrm{eq}}, \tag{7}$$

where ω^* is the rate of monomer addition to the critical cluster, Z is the Zeldovich factor[28] relating the equilibrium cluster-size distribution to the steady-state distribution, and $N_{n^*}^{\mathrm{eq}}$ is the equilibrium critical cluster concentration. The nucleation rate is expressed per unit time per unit volume.

In a series of thorough discussions[29–32] Reiss has shown that both the value of ω^* and of $N_{n^*}^{\mathrm{eq}}$ depend on the definition of a (critical) cluster. He argues that at present neither of the two values are known precisely. The classical theory does not properly account for the translational contribution to the cluster probability distribution, and introducing a fundamental volume scale is necessary to resolve the famous ''replacement free energy'' controversy that raged for almost 30 years.[33] Reiss tries to use computer experiments to generate and test reliable nucleation theories. In this work, we circumvent an independent calculation of ω^*, Z, and $N_{n^*}^{\mathrm{eq}}$, directly measuring the product I^S. It will turn out that remarkably accurate values of I^S are obtained when independently obtained thermodynamic and kinetic data of bulk phases and flat interfaces are substituted in a common-sense interpretation of Eq. (7), even though this expression is physically ill based.

The rate of monomer addition to the critical cluster is derived from measurements of the crystal growth rate (R):

$$R=\beta D\rho_s^{1/3}\frac{\Delta\mu}{kT}, \tag{8}$$

where β is a dimensionless kinetic coefficient and $\Delta\mu$ is the chemical potential difference between the liquid and solid phases, determined using Eq. (A1). Measurements of the crystal growth rate from the melt at constant pressure were reported in a previous paper,[34] and together with additional measurements of the crystal growth rate at a higher pressure[35] this results in the following fit for the kinetic coefficient:

$$\beta D\rho_s^{1/3}=(91.75+7.353P)D. \tag{9}$$

Using the reasonable assumption that the rate of addition of atoms to a growing crystal is similar to that for a spherical critical cluster, the expression for ω^* becomes

$$\omega^* = \beta D (6\pi^{1/2}\rho_s n^*)^{2/3}, \tag{10}$$

where n^* is the number of molecules contained in the critical cluster:

$$n^* = \frac{32}{3}\pi\left(\frac{\gamma}{\Delta\mu}\right)^3. \tag{11}$$

Here γ is the surface free energy per surface site. The expression for the rate constant ω^* is similar to that derived by Turnbull and Fisher[36] for condensed systems, but in Eq. (10) we replaced their unknown atomic jump distance by the measurable kinetic coefficient for crystal growth, making our estimates of the preexponential factor more reliable.

The Zeldovich factor (Z) is defined as[2]

$$Z = \sqrt{\frac{2\Delta\mu}{3\pi kTn^*}}, \tag{12}$$

and the equilibrium critical cluster concentration $N_{n^*}^{\mathrm{eq}}$ is defined as

$$N_{n^*}^{\mathrm{eq}} = \rho_l \exp\left(-\frac{\Delta G^*}{kT}\right), \tag{13}$$

where $\Delta G^*/kT$ is the free energy barrier defined as

$$\frac{\Delta G^*}{kT} = \frac{16\pi}{3}\frac{(\gamma/kT)^3}{(\Delta\mu/kT)^2}. \tag{14}$$

All parameters appearing in Eqs. (7)–(14) are well defined and can, at least in principle, be obtained from independent experiments. Since in practice the value of γ is not (yet) known precisely, we estimate γ by the empirical proportionality to the enthalpy of fusion (Δh) as found by Turnbull:[37]

$$\gamma = \psi\Delta h, \tag{15}$$

where Δh is the enthalpy difference between molecules of the liquid and solid phase. The proportionality constant ψ is about 0.46 for metals, 0.3 for semiconductors, water, etc., and 0.32 for a Lennard-Jones model similar to the one we use here.[38] We will use the parameter ψ as an empirical fit parameter in the expression for the nucleation PDF, Eq. (5).

By inserting Eqs. (10)–(15) into Eq. (7), the following expression for the steady-state classical nucleation rate is obtained:

$$I^S = 4\beta D\rho_s^{2/3}\sqrt{\psi\Delta h/kT}\,\rho_l \exp\left(-\frac{16\pi}{3}\frac{(\psi\Delta h/kT)^3}{(\Delta\mu/kT)^2}\right). \tag{16}$$

III. RESULTS AND DISCUSSION

A. Thermodynamic and self-diffusion measurements

In Fig. 1 the (P,T) phase diagram of the Lennard-Jones model is depicted, having a stable face-centered-cubic (fcc) solid region, a liquid region, and a vapor region (indicated in the inset). The boiling curve is a linear fit through a boiling point determined at $P=1.0$ atm (Ref. 39) ($T_b=74.1\pm1$ K), a boiling point determined at $P=20$ atm (Ref. 40) ($T_b=111.4\pm1$ K), and the value of the critical point ($P_c=51$ atm and $T_c=150\pm5$ K) as determined by Johnson *et al.*[41] for the truncated and shifted Lennard-Jones potential.

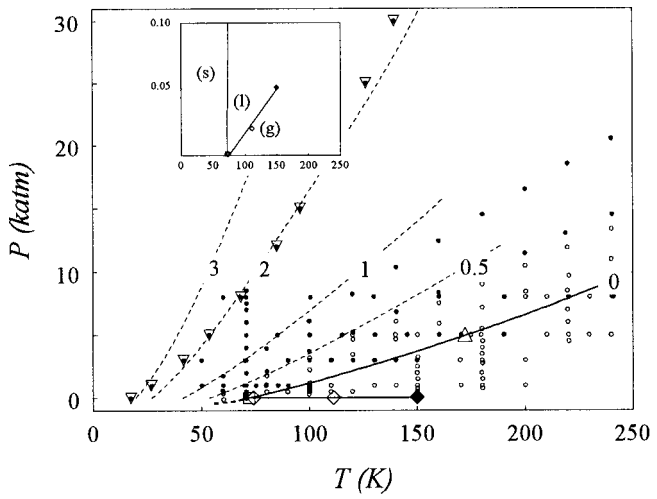

FIG. 1. The Lennard-Jones (P, T) phase diagram. In the inset the lower part of the pressure axis is enlarged with the solid (s), the liquid (l), and the vapor (g) regions indicated. The dashed curves indicated by 0, 0.5, 1, 2, and 3 are isochemical potential difference curves between the liquid and solid phases (i.e., $\Delta\mu/kT=$const). The contour indicated by 0 is the melting curve. The dashed curve is the extrapolation of $\Delta\mu=0$ into the vapor region. (□) The melting point used as reference point for the melting curve and (△) the melting point determined by simulations of crystal growth. (◇) Boiling points and (◆) critical point, connected by the boiling curve (solid line). At the points indicated as (●), equilibrium data have been obtained for the solid phase, at (○) for the bulk liquid phase, and at (▽) for the glass.

The reference point on the melting curve, indicated by 0 in Fig. 1, was $P_*=1.0$ atm and $T_*=72.0\pm0.5$ K, determined by thermodynamic integration[39] and later confirmed and refined by performing simulations of crystal growth from the melt[34] for the interaction potential of Eq. (1). A number of simulation runs for the solid as well as the liquid phase were performed at metastable conditions, where hystereses effects prevented melting or solidification.

In Fig. 1 five isochemical potential difference curves are shown, defined as $\Delta\mu/kT=\mu_s(\rho_s,T)/kT-\mu_l(\rho_l,T)/kT=C$, where the subscripts denote the liquid and solid phases, respectively. The melting curve is obtained for $\Delta\mu=0$.

As a test on the quality of the melting curve, we performed simulations of crystal growth at a pressure of 5 katm,[35] with a method identical to the simulation runs already performed at a pressure of 1 atm in Ref. 34. Eight simulation runs at $\Delta\mu<0.3kT$ were performed for the (100) and (110) as well as the (111) fcc orientation, resulting in an estimate of the melting point, i.e., the point $R=0$ in Eq. (8), of 172.2 ± 0.5 K. This is very close to our predicted value of 172.0 K, showing that the error in the melting curve is about 1 K.

The conditions for the ten simulation runs of the glass phase were all chosen on the line $D(\rho_l,T)=1\times10^{-5}$ nm^2/ns, where we expect that the atoms move less

than 1% of their diameter (σ) during the simulation run of 150 ps. The influence of the ten points in the glass phase on the melting curve was estimated by determining the melting curve without using these ten points. The predicted melting point at a pressure of 5 katm changed to 173.0 K, showing that the addition of the ten-points in the glass phase has a very small effect on the quality of our fits near the melting curve.

B. Homogeneous nucleation simulations

In order to estimate whether our number of atoms, 2002, is sufficient to eliminate detectable finite-size effects, we performed a series of nine simulation runs at a temperature of 92 K and a pressure of 3 katm with the number of atoms ranging from 125 to 10 000. At these conditions nucleation takes place with an average induction time that is within our simulation time limits.

Systems containing 500 atoms or less crystallized almost instantly (e.g., always within 0.05 ns), while systems containing 1000 or more atoms showed a detectable induction time, ranging from 0.13 ns to more than the complete simulation time (0.6 ns). There was no pattern in the induction time as function of the number of atoms, which is not surprising because we performed only six runs with a system containing more than 1000 atoms, while sampling the Poisson-distributed nucleation PDF. We therefore conclude that the most important and detectable finite-size effects are a much higher nucleation rate for systems containing less than 1000 atoms.

The results of the cooling and three heating simulation runs at a pressure of 3 katm are shown in Fig. 2. During the cooling run, the temperature is decreased by 300 K/ns. The measured temperatures as well as the applied temperature profiles (dashed curve) are shown, corresponding to each other up to the statistical noise. The density increases upon cooling, while the potential energy decreases, as shown in Figs. 2(b) and 2(c), following the predicted values for the liquid phase (dashed curves) closely up to a temperature of about 90 K. Below 90 K the density becomes slightly higher and the potential energy slightly lower than predicted.

When the temperature profile reached 80, 70, and 20 K the configuration from the cooling run was taken as the start of a heating run at the same heating rate. The heating run starting at 80 K did not show any sign of crystallization, resulting in the same path for the density and energy as function of temperature as for the cooling run, as shown in in Figs. 2(b) and 2(c). The other two heating runs, starting at 70 and 20 K, however, did show crystallization of the sample, evident from the deviations from the fit of the liquid density and potential energy. At the point where the deviation becomes large, a process named ''catastrophic crystal growth'' takes place.[11] It is attributed to system-size effects: e.g., the crystallites interact with themselves through the periodic boundary conditions, giving rise to a rapid completion of the solidification process. The nucleation process itself has taken place earlier, most probably during the cooling stage at a temperature between 70 and 80 K.

The density or potential energy of the crystallized samples never reached the density or potential energy of the perfect fcc crystal, shown as solid curves in Figs. 2(b) and 2(c), although the resultant crystal structure is always a mix of fcc and hcp structures (note that for a Lennard-Jones interaction potential the fcc and hcp structures are nearly degenerate[42]). The reasons are misalignment with respect to the simulation box, resulting in grain boundaries, the speed of the ''catastrophic crystal growth,'' inducing polycrystallinity as well as point defects and the fact that during some runs more than one critical cluster is formed, resulting in additional grain boundaries. In Fig. 2(b) the density of the crystals is approximately 1% less than the perfect fcc crystal density.

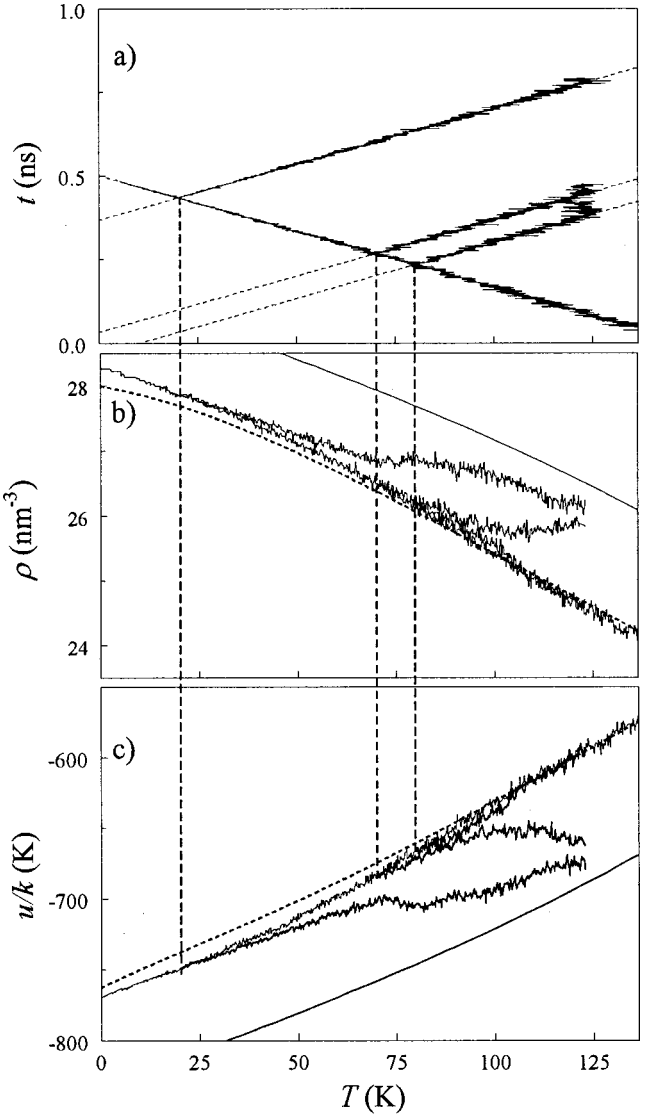

FIG. 2. (a) Example of simulation time (t) as function of the temperature (T) during a cooling run and three heating runs at $P=3$ katm. The dashed curves are the applied temperature profiles; the actual temperature during the runs is shown with solid lines. The cooling run started at $T=150$ K ($T_m=136$ K) and ended at $T=0$ K with a cooling rate of 300 K/ns. The heating runs started from the cooling run at $T=80$, 70, and 20 K (vertical dashed lines) and ended at $T=123$ K with a heating rate of 300 K/ns. (b) The number density (ρ) and (c) the potential energy (u/k) as a function of temperature for the heating and cooling runs. Solid curves in (b) and (c) are fits for the perfect fcc solid, while dashed curves are fits for the liquid.

The compression-decompression simulations produce profiles that are similar to the cooling-heating runs shown in Fig. 2. The internal pressure, measured during the simula-

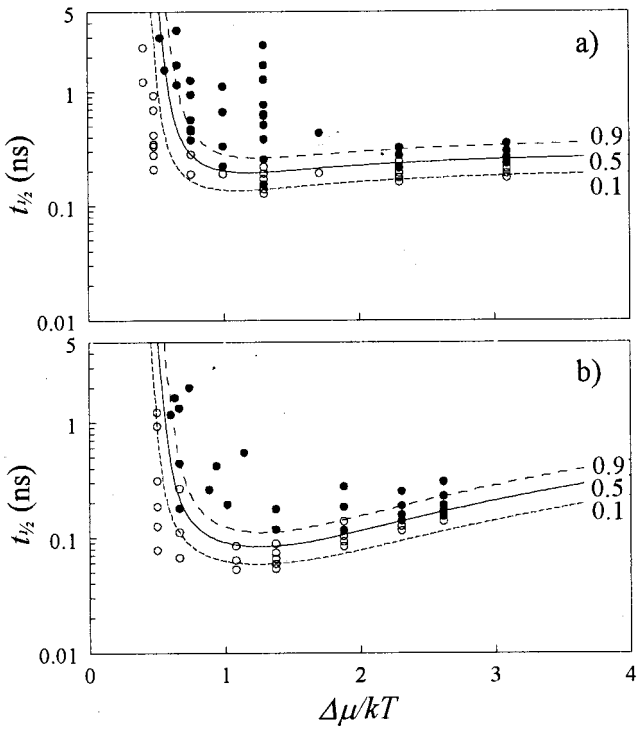

FIG. 3. The resulting phase [i.e., (●) crystalline phase, (○) liquid phase] as a function of the chemical potential difference and run time at maximum undercooling or compression. (a) For cooling-heating runs at a pressure of 3 katm and (b) for compression-decompression runs at a temperature of 100 K. Three nucleation PDF contours on the basis of fit T_B of Table III are shown with the probability indicated at the right of the curves.

tion, was always equal to the applied pressure (which changed linearly with time) even at the highest compression rates. The values of the density and potential energy relative to the predicted values where used to determine whether the system was in the solid or liquid phase at the end of the run.

The results for all cooling-heating runs at a pressure of 3 katm are shown in Fig. 3(a) and for all compression-decompression runs at a temperature of 100 K in Fig. 3(b). The runs that produced a crystalline phase are found at a higher chemical potential difference and longer simulation time. The reason is that at low chemical potential difference the system is in the metastable zone where the equilibrium critical cluster concentration N_{n*}^{eq} is very low, while at short simulation time the system has no time to nucleate [i.e., $t_{1/2}$ in Eq. (5) is close to zero]. The three isonucleation probability curves shown in Fig. 3 are taken from the fit of all data labeled T_B in Table III, below. They will be discussed in more detail below.

In Table I information about all cooling-heating runs at the five different pressures we used are shown, together with the quality of fit T_B of Table III that will be discussed in the next section. The ranges in chemical potential difference and time were similar for all series, but the temperature range and applied cooling rates increased with pressure. The same information for all compression-decompression runs at the five temperatures used are shown in Table II. Again, the ranges in chemical potential difference and time were similar for all series, but the pressure range and applied compression rates increased with temperature.

C. Application of empirical nucleation rate expressions

In order to find trends in the measurements of the nucleation probability, we applied two empirical fit equations to our data, labeled E_A and E_B in Table III. Our goal is to find a fit equation for $I(t)$ in Eq. (5) with a minimum number of fit parameters and a low value for S_{P_n} defined in Eq. (6).

The simplest possible one parameter fit equation, namely, $I(t)=C$, was used in fit E_A of Table III. The fit quality was 0.22, giving an upper limit for the value of S_{P_n} we must achieve with any reasonable expression for the nucleation rate. The value of fit parameter C gives a lower bound for the average nucleation rate found during the simulation runs.

The second empirical fit models the nucleation rate in the (P,T) phase diagram by a step function with three fit parameters, indicated by E_B in Table III. This equation qualitatively models the metastable zone for $0<\Delta\mu<\Delta\mu_{\mathrm{start}}$, followed by a zone of constant nucleation rate for $\Delta\mu_{\mathrm{start}}<\Delta\mu<\Delta\mu_{\mathrm{end}}$ and ended by a zero nucleation rate in the region where the molecular mobility is too low for $\Delta\mu>\Delta\mu_{\mathrm{end}}$. This results in a higher fit quality, showing that this model describes our data much better. The value of fit parameter C is more than twice as high compared to its value for fit E_A, as expected, giving a rough estimate for the nucleation rate found during the simulations where nucleation took place.

D. Application of classical nucleation theory

As a test of the applicability of steady-state classical nucleation theory to our nucleation probability measurements, we used Eq. (16) in Eq. (5). This results in a fit equation with only one parameter ψ. The results for this fit,

TABLE I. Summary of cooling-heating runs at constant pressure (P): the range in temperature at maximum undercooling (T), the applied cooling rates ($-dT/dt$), the maximum chemical potential difference ($\Delta\mu/kT$), the time at maximum undercooling ($t_{1/2}$), and the number of runs resulting in a liquid system (N_0) and in a solid system (N_1). Also shown is the quality of fit, S_{P_n}, for fit T_B of Table III.

P (katm)	T (K)	$-dT/dt$ (K/ns)	$\Delta\mu/kT$	$t_{1/2}$ (ns)	N_0	N_1	S_{P_n}
0.001	60.0–16.9	7.5–400	0.31–3.61	0.14–3.60	41	27	0.111
1	75.0–21.7	15–500	0.36–3.43	0.13–2.74	41	32	0.111
3	100.0–31.4	15–600	0.41–3.09	0.13–5.10	29	38	0.092
5	130.0–40.6	15–800	0.35–2.85	0.13–4.80	21	44	0.122
8	170.0–53.3	30–1000	0.32–2.64	0.09–4.06	21	36	0.139

TABLE II. Summary of cooling-heating runs at constant temperature (T): the range in pressure at maximum compression (P), the applied compression rates ($-dP/dt$), the maximum chemical potential difference ($\Delta\mu/kT$), the time at maximum compression ($t_{1/2}$), and the number of runs resulting in a liquid system (N_0) and in a solid system (N_1). Also shown is the quality of fit, S_{P_n}, for fit of Table III.

T (K)	T (katm)	$-dP/dt$ (katm/ns)	$\Delta\mu/kT$	$t_{1/2}$ (ns)	N_0	N_1	S_{P_n}
70	1.0–12.7	1.7–200	0.47–2.53	0.06–1.55	26	32	0.275
85	2.0–17.8	1.7–100	0.44–2.54	0.07–2.09	16	28	0.130
100	3.5–24.1	1.9–165	0.50–2.61	0.05–2.01	28	27	0.083
120	4.5–34.4	1.9–190	0.39–2.77	0.01–2.08	22	33	0.158
140	6.5–47.7	1.9–350	0.42–2.91	0.05–3.13	21	35	0.128

labeled N_A, are indicated in Table III. The value of ψ is in the correct range according to Turnbull,[37] but the value of S_{P_n} is higher than for fit E_A, showing that our measurements cannot be interpreted straightforwardly by steady-state classical nucleation theory.

In order to get a better estimate of the error in the expression for the steady-state classical nucleation rate, we added one additional fit parameter A to the preexponential factor:

$$I(t)=AI^s. \tag{17}$$

When steady-state classical nucleation theory applies to our data, the value of A should be close to 1. The result was the fit indicated by N_B in Table III. The fit quality is much improved by the second fit parameter, though still worse than obtained by the three-parameter step function E_B.

The value of ψ is in the correct range but now more compatible with the high heat of fusion materials. Approximately the same value was found by Broughton and Gilmer[38] who calculated the value for the surface free energy for the truncated and shifted Lennard-Jones potential at the triple point (e.g., $P\approx 1$ atm and $T\approx 72$ K). They found $\psi=0.32$ for the (111), (100), and (110) crystal-melt interfaces, which is close to our value of 0.28.

The value of fit parameter A is three orders of magnitude too small, showing that steady-state classical nucleation theory does not represent our data well. Therefore we expect that time-dependent effects in the nucleation rate, also called transient effects, are present.

E. Application of time-dependent nucleation theory

Time-dependent nucleation theory describes the nucleation rate as function of time, modeled by the evolution of an initial cluster-size distribution towards the cluster-size distribution at the steady-state nucleation rate.[1] Most analytical expressions for the time-dependent nucleation rate describe systems undergoing a sudden quench to a lower temperature, where the nucleation rate is zero at the beginning, increasing to the steady-state nucleation value at long times.[28,43–48] Other analytical expressions describe systems that are cooled at a constant cooling rate,[49–54] but with limited applicability due to severe approximations (one of the assumptions frequently made is the separation in time of crystal nucleation and growth, which is most probably not justified here). Numerical models have also been used, integrating the evolution of the cluster-size distribution in time directly.[1,55–57] Numerical calculations provide semiquantitative values for the time-dependent nucleation rate. Comparison between numerical methods and analytical expressions shows that the analytical expression derived by Kashchiev[43] produces a time dependence for the nucleation rate that is very close to numerical results.[1]

The treatment by Kashchiev is derived for isothermal conditions and does not assume the separation of nucleation and crystal growth in time. We will not discuss the details of his treatment here, but simply use the results

$$A=A(t)=1+2\sum_{m=1}^{\infty}(-1)^m\exp\left(-\frac{m^2t}{\tau}\right), \tag{18}$$

TABLE III. The results of the fits applied to the nucleation probability measurements: E_A and E_B are empirical fit equations, N_A and N_B are steady-state classical nucleation fit equations, and T_A and T_B are time-dependent nucleation fit equations. In the column $I(t)$ the applied fit formula is shown together with the corresponding fit parameters in the next column and the resulting fit quality expressed by S_{P_n}, defined in Eq. (6) in the last column.

Fit function	$I(t)$	Fit parameters			S_{P_n}
E_A	C	$C=0.042\ \mathrm{ns}^{-1}\,\mathrm{nm}^{-3}$			0.22
E_B	Step[a]	$C=0.097\ \mathrm{ns}^{-1}\,\mathrm{nm}^{-3}$	$\Delta\mu_{\mathrm{start}}=0.48kT$	$\Delta\mu_{\mathrm{end}}=2.2kT$	0.147
N_A: Eq. (16)	I^S	$\psi=0.42$			0.27
N_B: Eq. (17)	AI^S	$\psi=0.28$		$A=8.2\times10^{-4}$	0.160
T_A: Eq. (18)	$A(t)I^S$	$\psi=0.38$		$\tau=0.194$ ns	0.150
T_B: Eq. (18)	$A(t)I^S$	$\psi(\rho_l,T)=0.190+T/3.31\times10^{-5}+\rho_l/7.47\times10^{-3}$		$\tau=0.163$ ns	0.134[b]

[a] $I=C$ for $\Delta\mu_{\mathrm{start}}<\Delta\mu<\Delta\mu_{\mathrm{end}}$ and $I=0$ otherwise.

[b] See Tables I and II for values of S_{P_n} per series of nucleation probability measurements.

where Eq. (17) is used to express the time-dependent nucleation rate. Here τ is the transient time, also called the induction time, lag that sets the time scale for the time-dependent effects.

The time-dependent preexponential factor $A(t)$ describes the change in the nucleation rate over time after a sudden quench by an ''S-shaped'' curve starting with $A(0)=0$ with a long time limit of $A(\infty)=1$. In our system there is no sudden quench, but the system is evolving continuously. Therefore we replaced the total simulation time t in the expression for $A(t)$ by an effective time t^{eff} as an estimate of the time over which the nucleation conditions did not change appreciably:

$$t^{\text{eff}}(t)=\frac{\Delta\mu/kT}{\frac{\partial}{\partial t}(\Delta\mu/kT)}. \tag{19}$$

The effective time is large for slow cooling and compression runs and small for fast ones, and it turns out that $t^{\text{eff}}<t$ in all cases.

The transient time τ is used as a constant fit parameter. A short-time approximation for $A(t)$ is used when $t^{\text{eff}}<0.1\ \tau$, because of slow convergence of the sum at short-time scales. The resulting fit function contains two fit parameters: ψ in I^S and τ in $A(t)$. The fit is labeled T_A and the results are shown in Table III. It is the best two-parameter fit for our data. The value of ψ is again in the expected range, and the value of τ has the same order of magnitude as the simulation time for the highest cooling and compression rates (see Tables I and II). This shows that the time-dependent effects are strong in a large number of simulations and cannot be neglected.

Kashchiev obtained the expression $\tau=4/\pi^3\omega^* Z^2$ for the transient time at constant P and T, which is in the order of ps at the maximum of the nucleation rate for our system. This could mean that Eq. (19) overestimates t^{eff} by two orders of magnitude, but we also have to bear in mind that the expression for τ was derived by Kashchiev assuming constant P and T.

Until now the value of parameter ψ was taken to be independent of temperature and density. In order to include the dependence of ψ on T and ρ_l, we performed an additional fit where ψ is linear dependent on T and ρ_l. The results of this four-parameter fit, labeled T_B, are shown in Table III. It results in a value of $\psi=0.35$ at the triple point (e.g., $P\approx 1$ atm, $T\approx 72$ K, and $\rho_l=21.03\,\text{nm}^{-3}$), which is close to the value of $\psi=0.32$ calculated by Broughton and Gilmer.[38] The fit quality per series of simulation runs is shown in the last column of Tables I and II.

The time-dependent nucleation rate, Eq. (18), is a combination of the steady-state classical nucleation rate and a time-dependent preexponential factor. We can therefore use the results of fit function T_B to determine the steady-state classical nucleation rate. In Fig. 4 the steady-state classical nucleation rate is plotted in the (P,T) phase diagram. The maximum in the nucleation rate increases as a function of temperature and pressure, while the nucleation band broadens at the same time. This is in agreement with our findings that the maximum cooling rates that led to nucleation were much higher at higher pressure (Table I) and that the maximum compression rates that led to nucleation were much higher at higher temperature (Table II). The same effects were already observed by Clarke[58] who had difficulty preventing crystal nucleation during his study of the Lennard-Jones glass phase, when compressing a small sample of Lennard-Jones atoms at higher temperatures.

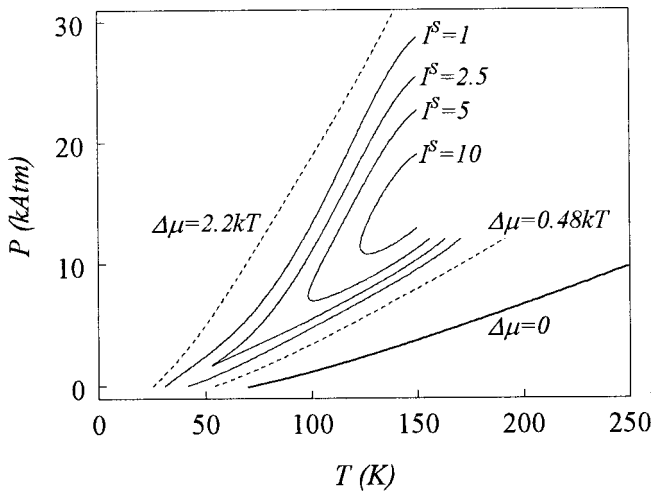

FIG. 4. The Lennard-Jones steady-state nucleation rate in a (P, T) diagram. The curve indicated by $\Delta\mu=0$ is the melting curve: the curves indicated by $I^S=1$, 2.5, 5, and 10 $\text{ns}^{-1}\,\text{nm}^{-3}$ are steady-state nucleation rate contours, calculated according to fit T_B of Table III. The dotted lines are the chemical potential contours of step fit function E_B of Table III.

Also indicated in Fig. 4 is the start and end chemical potentials of the step function E_B, showing that this fit equation tightly encloses the nucleation function I^S. The value of the step height of E_B is 0.097 $\text{ns}^{-1}\,\text{nm}^{-3}$, which is one or two orders of magnitude lower than a typical value of the maximum of I^S in Fig. 4, because E_B includes the effect of the transient time. This underlines the fact that the average time-dependent nucleation rate was about two orders of magnitude lower than the steady-state classical nucleation rate during our simulation runs.

In Fig. 5(a) the time-dependent nucleation rate is shown as a function of the chemical potential difference for three different cooling rates, together with the steady-state nucleation rate at $P=3$ katm. The nucleation rate is approximately equal to the steady-state nucleation rate when cooling at 15 K/ns with a maximum of 2.78 $\text{ns}^{-1}\,\text{nm}^{-3}$. At a cooling rate of 300 K/ns, the maximum nucleation rate dropped to 0.47 $\text{ns}^{-1}\,\text{nm}^{-3}$, while it was only 0.074 $\text{ns}^{-1}\,\text{nm}^{-3}$ at a cooling rate of 500 K/ns. The last value for the nucleation rate was also found when using the step function (E_B in Table III) to fit our data, showing that we experience strong transient effects during our simulations.

The nucleation PDF curves, calculated from the time-dependent nucleation rate by using Eq. (5), are shown in Fig. 5(b) at the same three cooling rates as shown in Fig. 5(a). The transition from zero to the maximum nucleation probability of one occurs very rapidly at a cooling rate of 15 K/ns, due to the large nucleation rate. At a cooling rate of 300 K/ns, the maximum of the nucleation PDF is lowered to 0.93, due to a lower nucleation rate and smaller physical time. The same trend is observed at a cooling rate of 500 K/ns, where the maximum of the nucleation PDF is only 0.21.

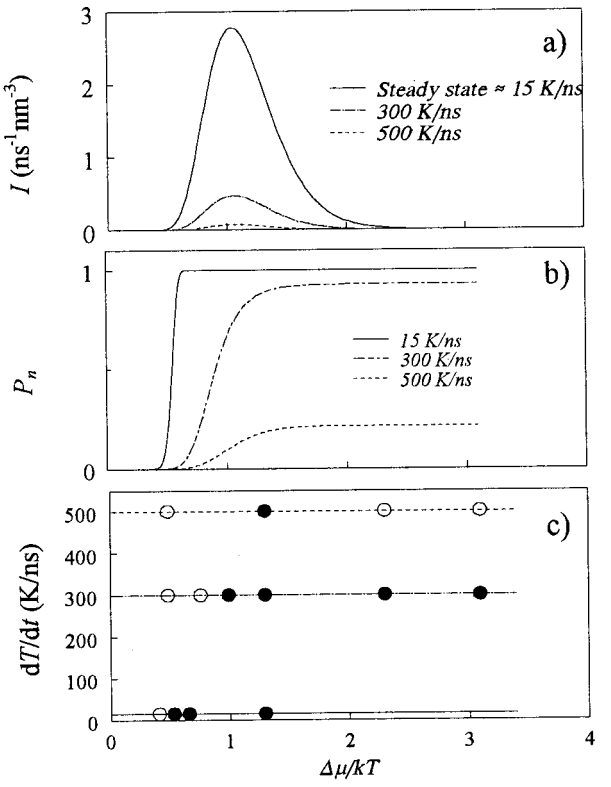

FIG. 5. (a) The nucleation rate according to fit T_B of Table III as a function of the chemical potential difference $(\Delta\mu/kT)$ at a pressure of 3 katm. Depicted are the steady-state nucleation rate, Eq. (16), and the time-dependent nucleation rate, Eq. (18), at three different cooling rates (note that the time-dependent nucleation rate at a cooling rate of 15 K/ns overlaps with the steady-state nucleation rate in the figure). (b) The nucleation PDF, Eq. (5), at the same three cooling rates as in (a) as a function of the maximum $\Delta\mu/kT$ reached during a cooling-heating sweep. (c) The resulting phase at the end of a simulation [i.e., (●) crystalline phase, (○) liquid phase] as a function of the cooling rate (dT/dt) and $\Delta\mu/kT$ at maximum undercooling. The results for the three cooling rates used in (b) are shown.

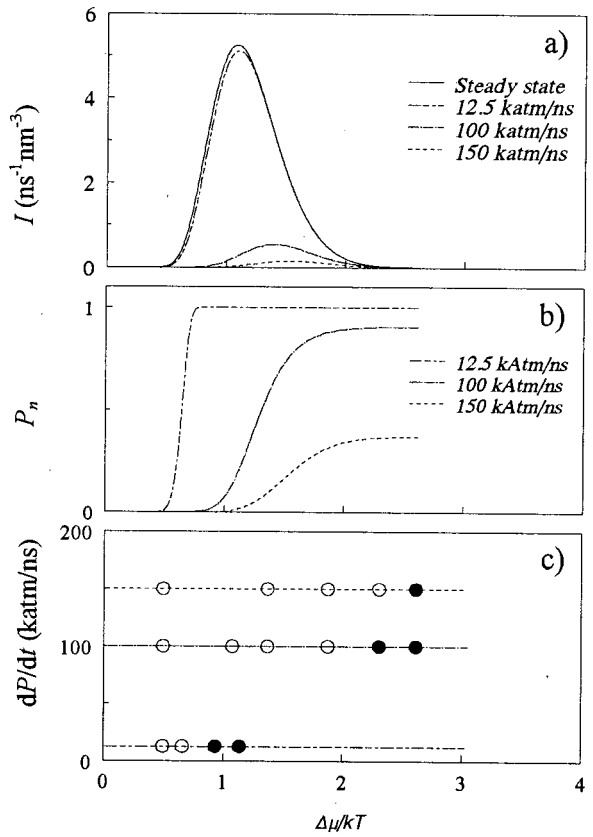

FIG. 6. (a) The nucleation rate according to fit T_B of Table III as a function of the chemical potential difference $(\Delta\mu/kT)$ at a temperature of 100 K. Depicted are the steady-state nucleation rate, Eq. (16), and the time-dependent nucleation rate, Eq. (18), at three different compression rates. (b) The nucleation PDF, Eq. (5), at the same three compression rates as in (a) as a function of the maximum $\Delta\mu/kT$ reached during a compression-decompression sweep. (c) The resulting phase at the end of a simulation [i.e., (●) crystalline phase, (○) liquid phase] as a function of the compression rate (dP/dt) and $\Delta\mu/kT$ at maximum compression. The results for the three compression rates used in (b) are shown.

The simulation results at the same cooling rates are shown in Fig. 5(c). The simulation results correlate very well with the nucleation PDF curves shown in Fig. 5(b), because at low nucleation probability the cooling-heating simulation runs often end in the liquid phase (open symbols), while at high nucleation probability they often end in the crystalline phase (solid symbols).

In Fig. 6 the same plots are shown for the compression-decompression runs at a temperature of 100 K. The plots are similar to Fig. 5, showing that the system has a similar nucleation behavior in cooling-heating runs and compression-decompression runs. The nucleation rate decreases as function of compression rate, shown in Fig. 6(a), starting at a maximum of 5.24 $ns^{-1}nm^{-3}$ for the steady-state nucleation rate. At a compression rate of 12.5 katm/ns, the maximum nucleation rate has dropped to 5.11 $ns^{-1}nm^{-3}$ at 100 katm/ns to 0.54 $ns^{-1}nm^{-3}$ and at 150 katm/ns to 0.154 $ns^{-1}nm^{-3}$ due to the transient effects.

The nucleation PDF curves, calculated from the time-dependent nucleation rate by using Eq. (5), are shown in Fig. 6(b) at the same three compression rates as shown in Fig. 6(a). The maximum nucleation probability decreases as a function of the compression rate from 1 at 12.5 katm/ns to 0.91 at 100 katm/ns to 0.37 at 150 katm/ns. The nucleation PDF curves predict the simulation results, shown in Fig. 6(c), very well: a low nucleation probability often results in a simulation ending in the liquid phase, while a high nucleation probability often results in a simulation ending in the crystalline phase.

In Figs. 3(a) and 3(b) three nucleation PDF contours are shown on the basis of fit T_B of Table III. The nucleation PDF curves shown in plots of Figs. 5(b)–5(d) and 6(b)–6(d) are slices from the same nucleation PDF hypersurface, but at a constant cooling or compression rate. The correlation between the nucleation PDF and the simulation results in Fig. 3 is excellent, showing that the time-dependent effects we measured are well described by Eq. (18).

From the contours in Fig. 3 we can find the minimum nucleation time for the Lennard-Jones liquid. The minimum simulation time before nucleation when linearly cooling or compressing a liquid is 0.1–0.3 ns, found at a chemical potential difference of about $1kT$ to $1.5kT$. Below $\Delta\mu \approx 1kT$

TABLE IV. Comparison between our data according to fit T_B of Table III and the calculated values for the nucleation rate by ten Wolde *et al.*, (Ref. 20) at two points in the phase diagram. Temperature and solid density data taken from ten Wolde *et al.*; values of other parameters at the two points in the phase diagram are determined by our thermodynamic fit equations. Characteristic values of the steady-state classical nucleation theory are given: the preexponential factor ($\omega^* Z \rho_l$), the value of the free energy barrier ($\Delta G^*/kT$), and the value of the steady-state nucleation rate (I^S).

	$T=68.5$ K, $P=0.62$ katm $\rho_l=23.28\ \mathrm{nm}^{-3}$, $\rho_s=25.38\ \mathrm{nm}^{-3}$ $\Delta\mu/kT=0.370$		$T=105.0$ K, $P=2.70$ katm $\rho_l=24.92\ \mathrm{nm}^{-3}$, $\rho_s=26.72\ \mathrm{nm}^{-3}$ $\Delta\mu/kT=0.282$	
	Our data	ten Wolde *et al.*	Our data	ten Wolde *et al.*
$\omega^* Z \rho_l\ (\mathrm{ns}^{-1}\,\mathrm{nm}^{-3})$	1.1×10^{4}	2.5×10^{5}	1.8×10^{4}	1.1×10^{5}
Δ^*/kT	24.7	19.4	30.3	24.1
$I^S\ (\mathrm{ns}^{-1}\,\mathrm{nm}^{-3})$	2.0×10^{-7}	9.4×10^{-4}	1.2×10^{-9}	1.4×10^{-6}

the simulation time increases rapidly, because the maximum nucleation rate is not reached as can be seen in Figs. 5 and 6. In order to keep a high nucleation probability in that region, the cooling or compression rate must be decreased. Below $\Delta\mu\approx0.5kT$ the situation becomes worse because even the steady-state nucleation rate is too low to nucleate the crystalline phase during the about 10 ns simulation time that is feasible during a computer simulation.

At $\Delta\mu>2.2kT$ the nucleation probability does not increase anymore during the cooling or compression simulations because of a low nucleation rate. If we define the glass transition as the line in the (P, T) phase diagram where the nucleation probability is 10% for a run of 10 ns length, then for our system containing 2002 particles the glass transition occurs where the nucleation rate is about $1\times10^{-4}\,\mathrm{ns}^{-1}\,\mathrm{nm}^{-3}$ (if we are able to quench the system with an infinite rate to the desired temperature and pressure). This line is found at $\Delta\mu\approx3kT$, resulting in a glass transition temperature of 17 K at a pressure of 1 atm. A cooling rate larger than 10^3 K/ns or a compression rate larger than 4×10^2 katm/ns must be used in order to prevent nucleation during a quench.

F. Comparison with other experimental and simulation work

A good example in literature of an experimental situation where the preexponential factor of the steady-state classical nucleation rate was found to be orders of magnitude too low is the paper by Brugmans and Vos.[15] They performed experiments where methanol was compressed to pressures up to 330 katm. Comparison between their measurements of the nucleation rate and steady-state classical nucleation theory revealed that the measured preexponential factor was about 10^{20} smaller than the predicted one. This large discrepancy leads one to suspect that time-dependent effects were also important in their experiments.

Ten Wolde *et al.* performed calculations of the nucleation rate at two points in the Lennard-Jones phase diagram, determining the free energy barrier for crystal nucleation by umbrella sampling and the preexponential factor by molecular dynamics simulations.[19,20] They used a somewhat different cutoff procedure than we did, but this can only introduce a small difference between the results.

The comparison between the calculations of ten Wolde *et al.* and our results are shown in Table IV The values of T and ρ_s are taken from the papers by ten Wolde *et al.*,[19,20] while the values of P, ρ_l, and $\Delta\mu/kT$ are determined with our thermodynamic fit equations. Characteristic data for the steady-state nucleation rate are given, all defined in Sec. II D.

The value of the preexponential factor ($\omega^* Z \rho_l$) differs one order of magnitude for both points, which is in our view a very good agreement for estimates of the nucleation rate. For our own data we already mentioned the error of a factor of 1–2 in the preexponential factor, due to the fact that we only took the cooling or compression stage into account in Eq. (5), but we expect a somewhat larger total error. The preexponential factor of ten Wolde *et al.* at the chemical potential difference of 0.370 is higher than the value at 0.282, which is unexpected for a kinetic preexponential factor. A preexponential factor is the usually largest at the melting curve, decreasing to zero at large chemical potential differences. Therefore we expect that the error in their preexponential factor is at least a factor of 2.

The values of the free energy barrier ($\Delta G^*/kT$) are also in close agreement with each other for both points shown in Table IV. The difference is approximately $5.3kT$ for both points, showing that the trend as a function of the chemical potential difference is identical. In our opinion these differences are acceptable in view of the intrinsic uncertainties in our method and the method of ten Wolde *et al.* (e.g., umbrella sampling).

The total steady-state nucleation rate (I^S) differs three orders of magnitude; one order of magnitude is introduced by the preexponential factor, while two orders of magnitude are introduced by the difference in the free energy barrier. One important point to note is the relatively large value of the nucleation rate at $T=68.5$ K calculated by ten Wolde *et al.* When applying their value for the nucleation rate to their system consisting of 10 648 particles with an average simulation time of 1.3 ns, the nucleation probability, Eq. (5), must have been 43%. With such a large value for the nucleation probability, the interpretation of their umbrella sampling data is not trivial. It is therefore likely that their calculations at $T=68.5$ K resulted in an overestimation of the actual nucleation rate.

IV. CONCLUSIONS

The thermodynamic parameters used in the expression for the nucleation rate were computed accurately for a large

range in temperature and pressure. Starting from an empirical expression for the chemical potential for both phases, all other thermodynamic parameters were obtained from exact thermodynamic relationships with the chemical potential.

Molecular dynamics simulations were used to measure the nucleation rate in the same range in temperature and pressure. By fitting the simulation results to analytical expressions for the steady-state nucleation rate, it was concluded that time-dependent effects played an important role in our simulations.

When including time-dependent effects in the expression for the nucleation rate, the correspondence between the measurements and analytical expression was excellent. By comparing the expression for the steady-state nucleation rate with the measurements, it was found that the time-dependent effects decrease the nucleation rate a factor of 10 on average in our simulations.

The resulting steady-state nucleation rate was comparable to the values calculated by others at two points in the phase diagram, as shown in Sec. III F. This led us to conclude that our method of determining the nucleation rate (from simulations where the system is cooled followed by heating or compressed followed by decompression at a constant rate) is capable of determining the nucleation rate over a wide range in temperature and pressure, without the need to recognize the critical cluster during the simulations.

Our results show that time-dependent effects have a large effect on the nucleation rate. Ignoring these effects results in a preexponential factor that can be orders of magnitude smaller than predicted by classical nucleation theory, as shown in Sec. III F. These time-dependent effects will not only play an important role during fast quenches (as performed in this paper), but in most measurements of the nucleation rate, because the transient time before the appearance of the first supercritical clusters scales with $(VI^S)^{-1}$. During this transient time, the cluster-size distribution present at the start of the experiment transforms to the distribution at the steady-state nucleation rate. The most accurate experiments that measure the nucleation rate are those that measure the occurrence of the first few supercritical clusters. In that case the transient effects cause a delay that is often ignored, resulting in an estimate for the preexponential factor that is orders of magnitude too low.

ACKNOWLEDGMENTS

H.E.A.H. acknowledges SENTER for financial support (Project No. BTS-98092). W. Kets is acknowledged for providing data about the growth rate of the Lennard-Jones potential at 5 katm and carefully reading the manuscript.

APPENDIX A: THERMODYNAMIC FIT EQUATIONS

The following expression for the dimensionless chemical potential (μ/kT) as a function of density and temperature was used:

$$\frac{\mu(\rho,T)}{kT}=\sum_{i,j=0}^{2}\mu_{ij}\rho^i T^{j-1}+\ln T\sum_{i=0}^{2}b_i\rho^i+\ln\rho\sum_{j=0}^{2}c_j T^{j-1}, \tag{A1}$$

where k is the Boltzmann constant and μ_{ij}, b_i, and c_i are the polynomial expansion coefficients.

The pressure is related to the chemical potential by[59]

$$\left(\frac{\partial}{\partial\rho}\frac{\mu(\rho,T)}{T}\right)_T=\frac{1}{\rho T}\left(\frac{\partial P(\rho,T)}{\partial\rho}\right)_T. \tag{A2}$$

This results in the following expression for the dimensionless pressure:

$$\frac{P(\rho,T)}{k\rho T}=\sum_{i,j=0}^{2}\frac{i}{i+1}\mu_{ij}\rho^i T^{j-1}+\ln T\sum_{i=0}^{2}\frac{i}{i+1}b_i\rho^i+\sum_{j=0}^{2}\left(c_j+\frac{p_j}{\rho}\right)T^{j-1}, \tag{A3}$$

where p_j are the polynomial fit parameters for the $P(0,T)$ curve.

The enthalpy is related to the chemical potential by[59]

$$\left(\frac{\partial}{\partial T}\frac{\mu(\rho,T)}{T}\right)_\rho=-\frac{h(\rho,T)}{T^2}+\frac{1}{\rho T}\left(\frac{\partial P}{\partial T}\right)_\rho. \tag{A4}$$

Together with Eqs. (A1) and (A3), this results in the expression for the dimensionless enthalpy:

$$\frac{h(\rho,T)}{kT}=\sum_{i,j=0}^{2}\frac{i-j+1}{i+1}\mu_{ij}\rho^i T^{j-1}+\sum_{i=0}^{2}\frac{i\ln T-1}{i+1}b_i\rho^i+\sum_{j=0}^{2}\left([j+(j-1)\ln\rho]c_j+\frac{jp_j}{\rho}\right)T^{j-1}. \tag{A5}$$

The parameter μ_{01} in Eq. (A1) remains unspecified when fitting Eqs. (A3) and (A5) together. Its value is fixed by requiring $\mu_s(\rho_s^*,T^*)=\mu_l(\rho_l^*,T^*)=0$ for the melting point at $T^*=72$ K indicated by the open squares in Fig. 1.

All measurements of the pressure and enthalpy are used in a combined fit procedure minimizing the quantity

$$S_\mu=wS_P+(1-w)S_h, \tag{A6}$$

where

$$S_P=\frac{1}{N}\sum_{n=1}^{N}\left(\frac{P(\langle\rho\rangle_n,T_n)-P_n}{k\langle\rho\rangle_n T_n}\right)^2$$

TABLE V. Fit parameter for μ, P, and h in Eqs. (A1), (A3), and (A5) for the solid phase, found by minimization of S_μ in Eq. (A6) with $w=0.5$. Also indicated is the fit error expressed by S_P and S_h of Eq. (A6).

j	0	1	2
μ_{0j}	-8.8276×10^4	3.2099×10^2	-5.5132×10^{-1}
μ_{1j}	-5.3454×10^3	-2.1041×10^1	-2.2242×10^{-3}
μ_{2j}	6.5020×10^1	2.7153×10^{-1}	-5.6350×10^{-5}
b_j	-6.3245	5.5500×10^{-1}	-1.6683×10^{-2}
c_j	5.5914×10^4	2.2055×10^2	1.9818×10^{-1}
p_j	-4.1618×10^5	-1.5479×10^3	-3.7877
S_P	6×10^{-4}		
S_h	8×10^{-4}		

TABLE VI. Fit parameter for μ, P, and h in Eqs. (A1), (A3), and (A5) for the liquid phase, found by minimization of S_μ in Eq. (A6) with $w=0.5$. Also indicated is the fit error expressed by S_P and S_h of Eq. (A6).

j	0	1	2
μ_{0j}	-3.4328×10^{4}	-8.5712×10^{2}	3.4693
μ_{1j}	-3.3125×10^{3}	-2.6264×10^{1}	1.9982×10^{-1}
μ_{2j}	5.0504×10^{1}	2.1196×10^{-2}	-2.3591×10^{-3}
b_j	1.5956×10^{1}	-3.0017	8.7894×10^{-2}
c_j	2.6273×10^{4}	4.7846×10^{2}	-2.1722
p_j	-1.5315×10^{5}	-3.6165×10^{3}	1.6357×10^{1}
S_P	1×10^{-2}		
S_h	1×10^{-2}		

and

$$S_h=\frac{1}{N}\sum_{n=1}^{N}\left(\frac{h(\langle\rho\rangle_n,T_n)-\langle h\rangle_n}{kT_n}\right)^2.$$

The summation runs over all N simulations performed for one phase, $\langle\rho\rangle_n$ and $\langle h\rangle_n$ denote the average density and enthalpy in simulation run n, respectively, and w is chosen between 0 and 1 and represents the weight of the pressure fit relative to that of the enthalpy fit.

The results of the fit procedure for $w=0.5$ are shown in Table V for the solid phase and in Table VI for the liquid phase. The fit results were insensitive to the value of w for $0.1<w<0.9$.

TABLE VII. Fit parameters d_{ij} for the self-diffusion in the liquid phase according to Eq. (B1). Also indicated is the fit error expressed by S_D of Eq. (B2).

$i\backslash j$	0	1	2
0	1.2929×10^{4}	-1.0269×10^{2}	2.4167×10^{-1}
1	-1.7496×10^{3}	1.3853×10^{1}	-3.0254×10^{-2}
2	7.9627×10^{1}	-6.1911×10^{-1}	1.3077×10^{-3}
3	-1.12301	9.3024×10^{-3}	-1.9297×10^{-5}
S_D	2×10^{-3}		

APPENDIX B: SELF-DIFFUSION FIT EQUATION

The expression for the self-diffusion coefficient as function of the density and temperature was

$$\ln[D(\rho,T)]=\sum_{i=0}^{3}\sum_{j=0}^{2}d_{ij}T^{j-1}\rho^{i}. \tag{B1}$$

All measurements of the liquid self-diffusion coefficient were used in Eq. (B1) minimizing the quantity

$$S_D=\frac{1}{N}\sum_{n=1}^{N}\left[\ln\left(\frac{D(\langle\rho\rangle_n,T_n)}{\langle D\rangle_n}\right)\right]^2, \tag{B2}$$

where $\langle D\rangle_n$ is the measured self-diffusion coefficient during simulation run n.

The fit coefficients found for the liquid self-diffusion coefficient are shown in Table VII together with the fit quality S_D.

[1] K. F. Kelton, in *Crystal Nucleation in Liquids and Glasses*, edited by H. Ehrenreich and D. Turnbull (Academic, Boston, 1991), Vol. 45, pp. 75–177.

[2] W. A. Tiller, *The Science of Crystallization: Microscopic interfacial phenomena* (Cambridge University Press, Cambridge, England, 1991).

[3] D. Frenkel and B. Smit, *Understanding Molecular Simulation* (Academic, London, 1996).

[4] D. Frenkel and J. P. McTague, Annu. Rev. Phys. Chem. **31**, 491 (1980).

[5] D. W. Oxtoby, Adv. Chem. Phys. **70**, 263 (1988).

[6] A. Rahman, M. J. Mandell, and M. J. McTague, J. Chem. Phys. **64**, 1564 (1976).

[7] M. J. Mandell, J. P. McTague, and A. Rahman, J. Chem. Phys. **64**, 3699 (1976).

[8] M. J. Mandell, J. P. McTague, and A. Rahman, J. Chem. Phys. **66**, 3070 (1977).

[9] J. D. Honeycutt and H. C. Andersen, Chem. Phys. Lett. **108**, 535 (1984).

[10] R. D. Mountain and A. C. Brown, J. Chem. Phys. **80**, 2730 (1984).

[11] J. D. Honeycutt and H. C. Andersen, J. Chem. Phys. **90**, 1585 (1986).

[12] S. Nosé and F. Yonezawa, J. Chem. Phys. **84**, 1803 (1986).

[13] F. Yonezawa, Solid State Phys. **45**, 179 (1991).

[14] W. C. Swope and H. C. Andersen, Phys. Rev. B **41**, 7042 (1990).

[15] M. J. Brugmans and W. L. Vos, J. Chem. Phys. **103**, 2661 (1995).

[16] J. S. van Duijneveldt and D. Frenkel, J. Chem. Phys. **96**, 4655 (1991).

[17] R. M. Lynden-Bell, J. S. van Duijneveldt, and D. Frenkel, Mol. Phys. **80**, 801 (1993).

[18] P. R. ten Wolde, M. J. Ruiz-Montero, and D. Frenkel, Phys. Rev. Lett. **75**, 2714 (1995).

[19] P. R. ten Wolde, M. J. Ruiz-Montero, and D. Frenkel, Faraday Discuss. **104**, 93 (1996).

[20] P. R. ten Wolde, M. J. Ruiz-Montero, and D. Frenkel, J. Chem. Phys. **104**, 9932 (1996).

[21] W. C. Swope, H. C. Andersen, P. H. Berens, and K. R. Wilson, J. Chem. Phys. **76**, 637 (1982).

[22] D. M. Heyes, Chem. Phys. **82**, 285 (1983).

[23] M. P. Allen and D. J. Tildesley, *Computer Simulation of Liquids* (Clarendon, Oxford, 1987).

[24] J. Q. Broughton and K. A. Jackson, Phys. Rev. Lett. **49**, 1496 (1982).

[25] H. E. A. Huitema and J. P. van der Eerden, J. Chem. Phys. **110**, 3263 (1999).

[26] J. J. Moré, B. S. Garbow, and K. E. Hillstrom, *User Guide for Minpack-1* (Argonne National Laboratory, Illinois, 1980).

[27] R. Becker and W. Döring, Ann. Phys. (N.Y.) **24**, 719 (1935).

[28] J. B. Zeldovich, Acta Physicochim. URSS **18**, 1 (1943).

[29] P. G. Debenedetti and H. Reiss, J. Chem. Phys. **108**, 5498 (1998).

[30] B. Senger, P. Schaaf, D. S. Corti, R. Bowles, J. C. Voegel, and H.

Reiss, J. Chem. Phys. **110**, 6421 (1999).
[31] B. Senger, P. Schaaf, D. S. Corti, R. Bowles, D. Pointu, J. C. Voegel, and H. Reiss, J. Chem. Phys. **110**, 6438 (1999).
[32] H. Reiss and R. K. Bowles, J. Chem. Phys. **111**, 7501 (1999).
[33] H. Reiss, W. K. Kegel, and J. L. Katz, J. Phys. Chem. A **102**, 8548 (1998).
[34] H. E. A. Huitema, M. J. Vlot, and J. P. van der Eerden, J. Chem. Phys. **111**, 4714 (1999).
[35] W. Kets, H. E. A. Huitema, and J. P. van der Eerden (private communication).
[36] D. Turnbull and J. C. Fisher, J. Chem. Phys. **24**, 719 (1935).
[37] D. Turnbull, in *Thermodynamics in Physical Metallurgy* (ASM, Cleveland, 1950).
[38] J. Q. Broughton and G. H. Gilmer, J. Chem. Phys. **84**, 5759 (1986).
[39] M. J. Vlot, J. C. van Miltenburg, H. A. J. Oonk, and J. P. van der Eerden, J. Chem. Phys. **107**, 10 102 (1997).
[40] M. J. Vlot, S. Claassen, H. E. A. Huitema, and J. P. van der Eerden, Mol. Phys. **91**, 19 (1997).
[41] J. K. Johnson, J. A. Zollweg, and K. E. Gubbins, Mol. Phys. **78**, 591 (1993).
[42] E. Burke and J. Q. Broughton, J. Chem. Phys. **89**, 1030 (1988).
[43] D. Kashchiev, Surf. Sci. **14**, 209 (1969).
[44] F. C. Collins, Z. Elektrochem. **59**, 404 (1955).
[45] A. Kantrowitz, J. Chem. Phys. **19**, 1097 (1951).
[46] H. Wakeshima, J. Chem. Phys. **22**, 1614 (1954).
[47] B. K. Chakraverty, Surf. Sci. **4**, 205 (1966).
[48] J. Feder, K. C. Russell, J. Lothe, and G. M. Pound, Adv. Phys. **15**, 111 (1966).
[49] R. W. Hopper, G. Scherer, and D. R. Uhlmann, J. Non-Cryst. Solids **15**, 45 (1974).
[50] V. A. Sneidmann and M. C. Weinberg, J. Non-Cryst. Solids **194**, 145 (1996).
[51] V. A. Sneidmann, J. Appl. Phys. **80**, 803 (1996).
[52] V. A. Sneidmann and D. R. Uhlmann, J. Chem. Phys. **108**, 1094 (1998).
[53] V. A. Sneidmann and D. R. Uhlmann, J. Chem. Phys. **109**, 186 (1998).
[54] V. A. Sneidmann, Phys. Rev. E **59**, 4441 (1999).
[55] K. F. Kelton and A. L. Greer, J. Non-Cryst. Solids **79**, 295 (1986).
[56] K. F. Kelton, J. Non-Cryst. Solids **163**, 283 (1993).
[57] K. F. Kelton, K. Lakshmi Narayan, L. E. Levine, T. C. Cull, and C. S. Ray, J. Non-Cryst. Solids **204**, 13 (1996).
[58] J. H. R. Clarke, J. Chem. Soc., Faraday Trans. 2 **75**, 1371 (1979).
[59] D. A. McQuarrie and J. D. Simon, *Physical Chemistry: A molecular approach* (University Science Books, Sausalito, 1997).